Detection of Flooded Areas Caused by Typhoon Hagibis by Applying a Learning-Based Method Using Sentinel-1 Data

Takahiro Igarashi and Hiroyuki Wakabayashi, *Member, IEEE*

***Abstract*—Typhoon Hagibis (No. 19, in Japan) made landfall in Koriyama City in Fukushima Prefecture, Japan, on October 13, 2019. The consequent floods damaged built-up areas in the city center. Furthermore, rice production was affected because the flood occurred before rice harvesting. Although the effects of inundation using Sentinel-1 synthetic aperture radar (SAR) data have been studied, further quantitative analyses are necessary to detect flooded areas using SAR data because the changes in the backscattering coefficient are complex and vary between built-up and paddy areas. Here, we aimed to apply a learning-based method to detect flood-damaged areas in both built-up areas and paddy fields. The training and test datasets were derived from variations in backscattering coefficients measured by Sentinel-1 SAR before and during the flooding event. Moreover, changes in SAR data in built-up areas and paddy fields, where flood damage occurred, were used as training data. A support vector machine was applied as a classifier to detect areas damaged by floods. The proposed method can detect flood-damaged areas caused by Typhoon Hagibis in both the built-up and paddy areas. Changing both the backscattering coefficient and texture (entropy) information improved the flood detection accuracy by a kappa coefficient of 0.15 when compared with that achieved using backscattering-only input. Furthermore, upon comparing *F*-values across categories using dual and single polarization, we found that VV (transmit V and receive V polarizations) enhanced the accuracy of detecting flooded built-up areas, while VH (transmit V and receive H polarizations) yielded improvements in identifying flooded paddy areas.**

***Index Terms*—Backscattering coefficient, entropy, flooded area detection, gray-level co-occurrence matrix (GLCM), support vector machine (SVM).**

I. Introduction

TYPHOON Hagibis (No. 19, 2019) made landfall in Japan on October 12, 2019. Many areas through which the typhoon passed, such as Kanto, Koshin, and Tohoku, were heavily damaged by floods. In the southern part of the Tohoku region, several flooding events occurred in the Abukuma River Basin, causing considerable damage in built-up areas. For example, in Koriyama City, Fukushima Prefecture, Abukuma River and its tributaries, such as the Sasahara, Yata, and Ouse Rivers, caused inundation above the floor in 6931 cases and inundation below the floor in 956 cases [1]. In addition, rice production was adversely affected because flooding occurred in paddies in the Tohoku region before the harvest period [2], [3].

Sentinel-1B captured data in the early morning (5:42 JST) on October 13, 2019, when the flooded area was the largest, covering Koriyama City and its surroundings. Therefore, this satellite was suitable for analyzing the effects of inundation on synthetic aperture radar (SAR) data. The initial analysis examined the changes in backscattering coefficient and coherence in flooding areas using Sentinel-1 SAR data [4]. However, a quantitative analysis over a broader area is necessary to accurately detect areas that are affected by flooding, including built-up areas and paddy fields. To the best of the knowledge of the authors, only a few studies on the high-precision detection of flooding areas that encompass both built-up areas and paddy fields are available [5], [6].

When the water level in the paddies exceeds the plant height, the dominant backscattering mechanism of the smooth water surface exhibits specular reflection. Therefore, a fully flooded paddy field observed by SAR shows lower backscattering coefficients than nonflooded paddies. Many methods have been proposed to optimize the backscatter threshold [7], [8], [9], such as split-based automatic thresholding applied to TerraSAR-X data [10], a combination of image segmentation and the surface scattering model applied to CosmoSkyMed *X*-band SAR data [11], and an automated Sentinel-1-based processing chain designed for flood detection and monitoring in near real time [12].

When flooding occurs in built-up areas, such as urban or residential areas, double-bounce scattering between the building wall and the water surface increases. However, because the change in the backscattering coefficient is complex and depends on the azimuthal angle of the building wall, radar incidence angle, and vegetation cover on the ground, the same thresholding method usually cannot be applied to built-up areas. An alternative method for detecting inundation areas is to use coherence calculated using interferometric SAR analysis. Coherence can recognize changes in the backscattering mechanism between

Manuscript received 15 September 2023; revised 9 March 2024; accepted 8 May 2024. Date of publication 13 May 2024; date of current version 30 May 2024. This work was supported in part by the Japan Society for the Promotion of Science Grants-in-Aid for Scientific Research under Grant JP22KK0089 and in part by the Center for Environmental Remote Sensing, Chiba University. *(Corresponding author: Hiroyuki Wakabayashi.)*

Takahiro Igarashi is with the Graduate School of Engineering, Nihon University, Koriyama 963-8642, Japan (e-mail: ceta21001@g.nihon-u.ac.jp).

Hiroyuki Wakabayashi is with the Graduate School of Human Informatics, Tohoku Gakuin University, Sendai 984-8588, Japan (e-mail: hwaka@mail.tohoku-gakuin.ac.jp).

Digital Object Identifier 10.1109/JSTARS.2024.3400282

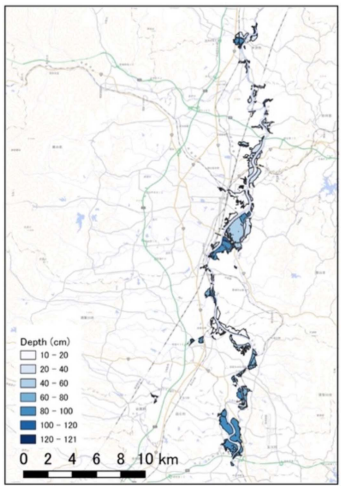

Fig. 1. Inundation depth map created and provided by the GSI.

two data acquisition intervals. It decreases in flooded, urban, and vegetated areas [6], [13], [14], [15]. However, because coherence calculates the phase correlation between two observations, at least three observations are needed to detect the flooded area, for example, two before and one during flooding. In addition to the aforementioned methods that use backscattering and coherence changes, texture information derived from the gray-level co-occurrence matrix (GLCM) [16] can improve the accuracy of flood detection [17], [18].

This study applied a learning-based approach to detect built-up areas and paddies affected by floods caused by Typhoon Hagibis using the changes in backscattering coefficients before and during flooding. Specifically, built-up areas and paddies in Koriyama City, which were affected by flooding, were used as training data. By training a learning-based classifier on the changes in backscattering coefficients caused by flooding and applying the trained model to the test data, flood-affected areas were detected. In addition, the research leveraged texture information computed from the GLCM to enhance flood detection accuracy.

II. Test Site and Sentinel-1 Data

In Koriyama City, the urban area is in the city center and is surrounded by agricultural areas. Because the Abukuma River flows through the city center from south to north, flood damage in 2019 was concentrated near this river.

This study selected flooded and nonflooded areas based on the inundation depth map [19] released by the Geospatial Information Authority of Japan (GSI). The map shown in Fig. 1 presents the inundation depth characterized by different shades of blue. The depths were calculated using elevation data and aerial photographs taken by the GSI on October 13, 2019 [20]. Fig. 2 shows aerial photographs of the Koriyama City Center captured in the afternoon (JST) on October 13, 2019, along with the flooded areas on the inundation depth map.

Based on the inundation depth map, we manually set polygons for built-up areas and paddy fields. Four categories were established: flooded built-up areas, flooded paddy fields, nonflooded

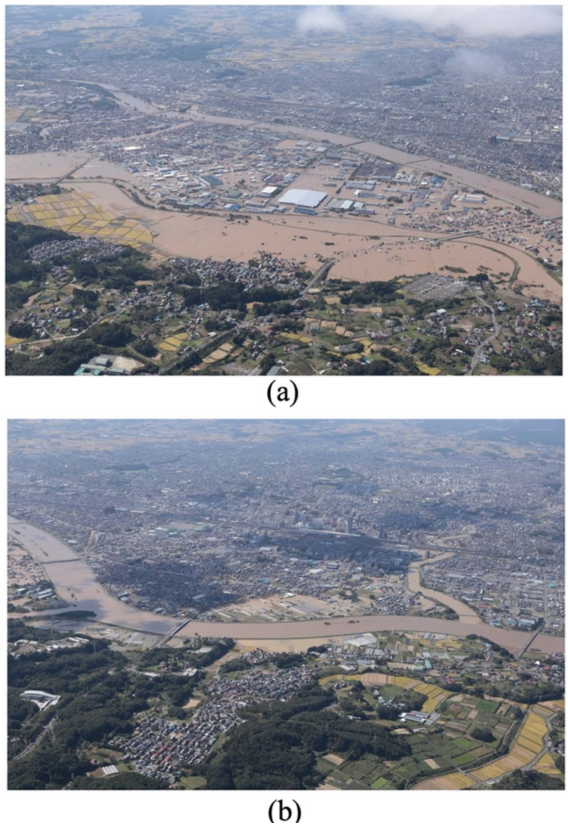

Fig. 2. Aerial photographs taken by the GSI around noon on October 13, 2019. These bird-eye views were captured from the east side of Koriyama City and by facing the west direction. (a) Southern part of the Koriyama City Center. (b) Northern part of the Koriyama City Center.

TABLE I
Summary of Sentinel-1 Data Characteristics

Platform	Sentinel-1A	Sentinel-1B
Acquisition time	5:43 A.M. 7 October(JST)	5:42 A.M. 13 October(JST)
Orbit direction	Descending	Descending
Observation mode	IWS	IWS
Polarization	VV + VH	VV + VH
Resolution (Range × Azimuth)	5 m × 20 m	5 m × 20 m

built-up areas, and nonflooded paddy fields. Fig. 3 shows the training and test areas indicated by the categories used to extract the inundation areas in this study.

Interferometric wide (IW) swath mode data from Sentinel-1A and Sentinel-1B observed at the test site on the mornings of October 7 and 13, 2019, were applied as the SAR data. Table I summarizes the characteristics of the Sentinel-1 data used in the analysis. The IW mode employs terrain observation with the progressive scan SAR technique [21] to acquire data over a 250-km swath with a spatial resolution of approximately 5 m (range) $\times$ 20 m (azimuth) in the slant range. The incident angle ranged from 29° to 46° in the IW mode. Koriyama City is located at an incidence angle of approximately 35°. Dual-polarization data,

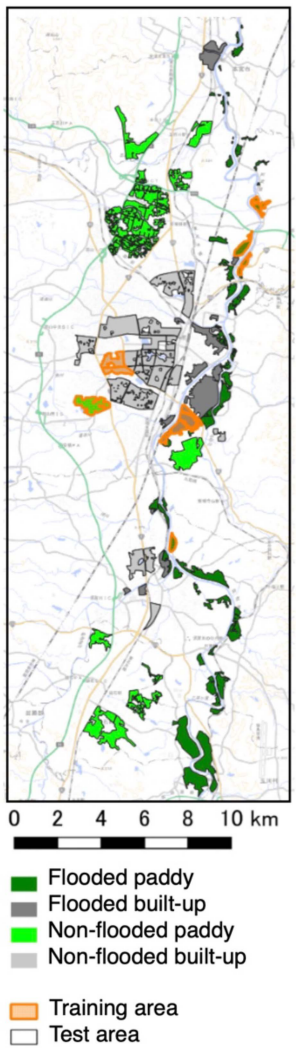

Fig. 3. Training and test areas selected in this study based on the inundation depth map given in Fig. 1.

VV (transmit V and receive V polarization) and VH (transmit V and receive H polarization), were acquired.

III. Sentinel-1 Data Preprocessing and Analysis

A. Preprocessing of Sentinel-1 Data

The European Space Agency Copernicus Open Access Hub provided Level-1 Ground Range Detected (GRD) data for backscattering analysis, along with the Sentinel Toolbox to preprocess the GRD data.

After obtaining high-precision orbital data, we applied thermal noise removal and radiometric calibration to the gamma naught (γ^0) with terrain flattening of the GRD data. γ^0 was used instead of the backscattering coefficient (σ^0) to reduce the sensitivity to the effect of incidence angle. Finally, the data were projected onto Universal Transverse Mercator coordinates (Zone 54) with a pixel spacing of 10 m. The Shuttle Radar Topography Mission digital elevation model with a 1-arc-second (30 m) grid was applied for both radiometric terrain flattening and orthorectified processing.

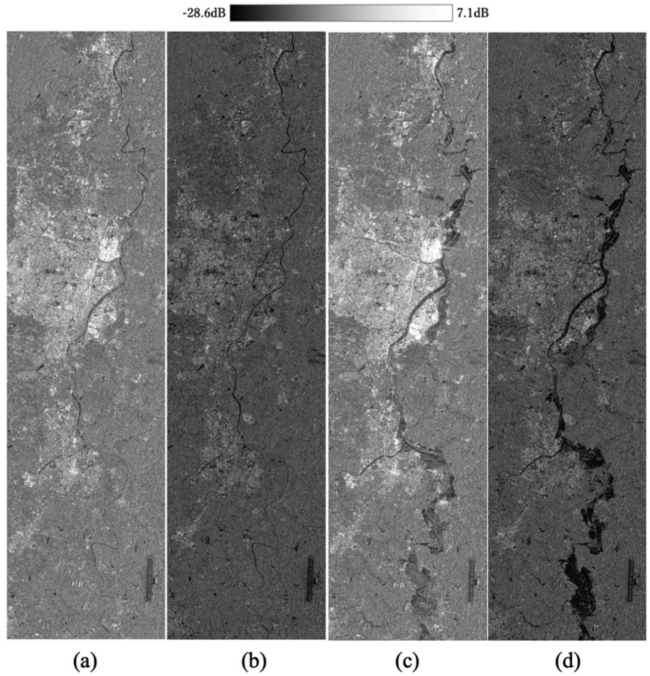

Fig. 4. Eight-bit scaled and cutout $\gamma 0$ images (972 pixels by 3739 lines). (a) VV and (b) VH images acquired on October 7, 2019. (c) VV and (d) VH images acquired on October 13, 2019.

The Sentinel Toolbox created γ^0 images with a wide dynamic range, representing each pixel in a 32-bit floating format. To calculate the GLCM elements, scaling the pixel values and adjusting the number of gray levels is necessary. Therefore, the maximum and minimum values were obtained from the 98% range, excluding the top and bottom 1% of image histograms, and resulted in a range from -28.6 to 7.1 dB. Fig. 4 shows the scaled (256 levels) Sentinel-1 images covering our test site.

B. Texture Calculation

Each element (*i*th row and *j*th column) in the GLCM represented the relative occurrence of two different gray levels using pixels that were separated by a fixed distance (Δx, Δy), and the statistics calculated from the GLCM elements provide quantitative textural information. When the calculation window size was $N \times M$, each element of the GLCM was calculated as follows:

$$P(i,j:\Delta x,\Delta y)=\frac{1}{2(N-\Delta x)(M-\Delta y)}\{Q(i,j:\Delta x,\Delta y)+Q(j,i:\Delta x,\Delta y)\} \tag{1}$$

$$Q(i,j:\Delta x,\Delta x)=\sum_{n=1}^{N-\Delta x}\sum_{m=1}^{N-\Delta y}A$$

$$A=\begin{cases}1, & I(n,m)=i\wedge I(n+\Delta x,m+\Delta y)=j\\ 0, & \text{elsewhere}\end{cases} \tag{2}$$

where $Q(i, j: (\Delta x, \Delta y)$ represents the number of pixels that have gray level j at a distance of $(\Delta x, \Delta y)$ away from the corresponding pixel (gray level i) within the calculation window, and I (n, m) represents the gray-level value at coordinates (n and m) in the calculation window. In this study, the values in the four directions (1,0), (1,1), (0,1), and $(-1,1)$ were averaged as $(\Delta x, \Delta y)$ to calculate GLCM elements. Due to the different spatial resolutions of Sentinel-1 GRD, which are 5 m in the range direction and 20 m in the azimuth direction, the average of four directions is used for the calculation of the GLCM element. Subsequently, texture features were calculated using the above GLCM elements and used as the support vector machine (SVM) input vector.

The texture information, namely, entropy, was calculated using the GLCM. Entropy (ENT), which is the most useful texture feature for land cover classification [22], can be calculated from the GLCM elements as follows:

$$\mathrm{ENT} = -\sum_{i,j} P(i,j) \log P(i,j). \tag{3}$$

C. Leaning-Based Classification to Detect the Flood Area

The SVM is a supervised learning algorithm that focuses on training samples closest to an optimal boundary among feature space classes [23]. This algorithm maximizes the distance between the training samples and discrimination boundary and improves the generalization performance. The SVM is widely used in land cover classification that uses remotely sensed data. Compared to other commonly used learning classifiers, this algorithm can perform well with relatively small training datasets [24], [25]. We used a library for support vector machine (LIBSVM) [26] as the SVM library to classify nonflooded and flooded areas. The LIBSVM supports C-support vector classification [26], with radial basis function serving as the kernel function [25], [26]. In this analysis, the hyperparameters (cost and gamma) of the SVM were tuned using a grid search [22] with stratified fivefold cross validation [26], [27].

While selecting the training areas, adjustments were made to ensure minimal differences in the acquired pixel count of the training areas of each category. Five locations were selected from flooded paddy fields, two from flooded built-up areas, one from nonflooded paddy fields, and one from nonflooded built-up areas, and the sample pixel numbers for these training areas were 9158, 9221, 8403, and 8327, respectively. The acquired training data were imbalanced; thus, duplicate data were removed, and each category was weighted during the SVM training to mitigate the impact of imbalanced data on the learning results.

Fig. 5 summarizes the procedure employed for detecting flooded areas. Four feature vectors were prepared for the input vector data in the SVM classification procedure (see Fig. 6). Vector 1 comprised dual-pol γ^0 (VV and VH) before and during flooding. Vector 2 comprised texture information before and during flooding, in addition to Vector 1. Finally, Vectors 3 and 4 comprised only single-pol γ^0 (VV or VH) and its texture information. Each element in the input vectors was normalized from -1 to 1 using the minimum and maximum values.

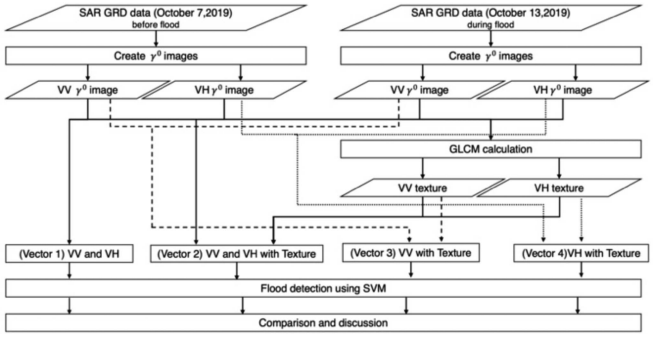

Fig. 5. Procedure for detecting flooded areas.

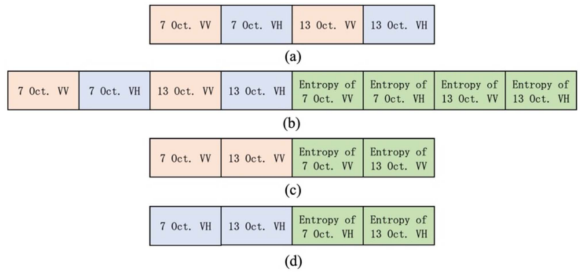

Fig. 6. Configuration of input vectors. (a) Vector 1. (b) Vector 2. (c) Vector 3. (d) Vector 4.

The effectiveness of the texture information was evaluated by comparing the detection accuracies of flooded areas by Vectors 1 and 2. In addition, by comparing the detection accuracies of flooded areas using Vectors 2 and 3, and Vectors 2 and 4, the contribution of VV and VH polarizations to flooded area detection accuracy could be evaluated.

We changed the gray level and window size to calculate the GLCM, with gray levels of 2, 4, 8, and 16, and window sizes of 3×3, 7×7, 11×11, 15×15, and 19×19. The combination with the highest flooded area detection accuracy in the test area was selected for further analysis.

D. Accuracy Assessment for Detecting Flooded Areas

Fig. 7 illustrates the procedure for calculating accuracy in detecting flooded areas. In Vector 1 [see Fig. 7(a)], a learning model was tuned using data pertaining to the training area, and the detection accuracy was estimated for both the training and test areas. Vectors 2–4 [see Fig. 7(b)] involved the development of 20 types of training and test data, varying in gray level and window size for calculating the GLCM as described in Sections III-C, generated according to the scheme in Fig. 7(c). Each learning model was then tuned using the training data [see Fig. 7(d)]. The combination of gray level and window size that yielded the highest detection accuracy in the test area was selected. Finally, the detection accuracies of flooded areas in the training and test areas were compared across the four vectors.

We used the kappa coefficient calculated from the flooded area detection results for all the categories. We also used the F1 score (F-value) calculated from the flooded area detection results to evaluate the accuracy of each category.

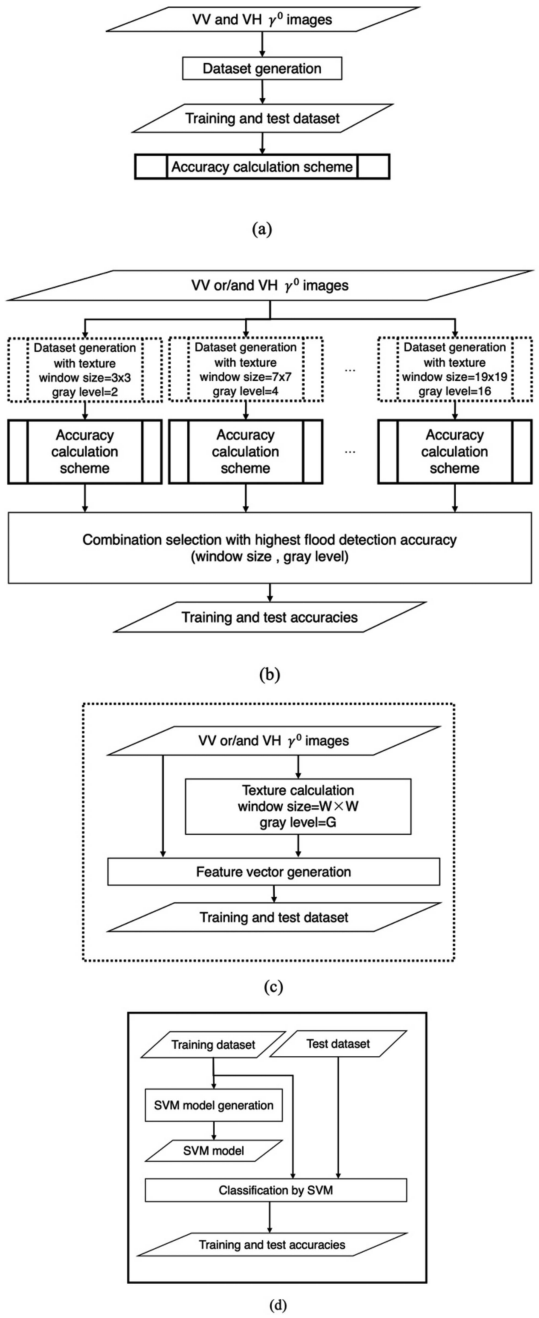

Fig. 7. Procedure of calculating the detection accuracies for flooded areas. (a) Vector 1. (b) Vectors 2–4. (c) Dataset generation scheme. (d) Accuracy calculation scheme.

TABLE II
SUMMARY OF FLOOD DETECTION ACCURACIES FOR VECTORS 1–4

Vector				1	2	3	4
				γ^0	γ^0+Texture	γ^0+Texture	γ^0+Texture
				VV+VH	VV+VH	VV	VH
Training area	Kappa			0.763	0.993	0.914	0.894
	F1	Flooded areas	paddy	0.881	1.000	0.936	0.993
			built-up	0.794	0.990	0.938	0.857
		Non-flooded areas	paddy	0.820	0.999	0.932	0.944
			built-up	0.791	0.988	0.937	0.84
Test area	Kappa			0.615	0.763	0.657	0.708
	Gray level Window size			—	8 19×19	2 19×19	16 19×19
	F1	Flooded areas	paddy	0.747	0.894	0.769	0.884
			built-up	0.508	0.583	0.531	0.515
		Nonflooded areas	paddy	0.755	0.904	0.790	0.843
			built-up	0.754	0.822	0.798	0.787

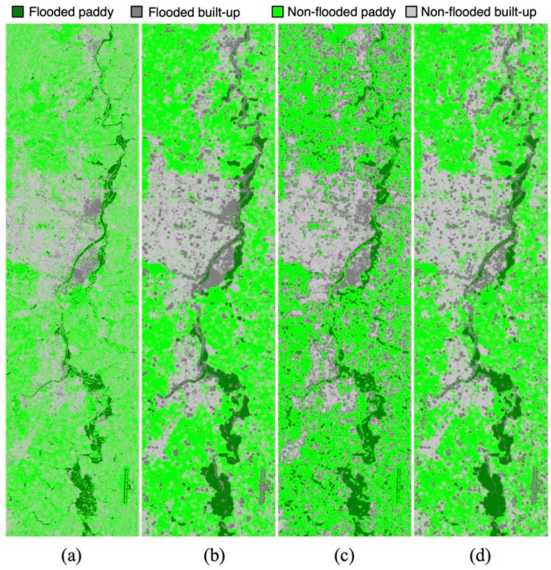

Fig. 8. Classified images with the highest flood detection accuracies for (a) Vector 1, (b) Vector 2, (c) Vector 3, and (d) Vector 4.

TABLE III
SUMMARY OF KAPPA COEFFICIENTS RELATED TO WINDOW SIZE AND GRAY LEVEL

		Kappa coefficient				
		Window size				
Vector	Gray level	3×3	7×7	11×11	15×15	19×19
2	2	0.613	0.627	0.647	0.668	0.673
	4	0.641	0.661	0.701	0.729	0.731
	8	0.630	0.671	0.703	0.745	0.763
	16	0.617	0.666	0.707	0.742	0.755
3	2	0.520	0.571	0.614	0.642	0.657
	4	0.535	0.576	0.595	0.614	0.610
	8	0.532	0.568	0.586	0.608	0.636
	16	0.524	0.562	0.585	0.623	0.627
4	2	0.499	0.548	0.574	0.576	0.592
	4	0.504	0.574	0.633	0.646	0.638
	8	0.465	0.550	0.607	0.671	0.684
	16	0.470	0.543	0.620	0.681	0.708

IV. RESULTS AND DISCUSSION

A. Accuracy Improvement of Flood Detection by Combining Texture Information

Table II summarizes the flood detection accuracies using Vectors 1–4, and Fig. 8 shows the corresponding flood-detected images. When comparing the detection accuracy of the flooded area using the various input data shown in Table II, the kappa coefficient in the test area for Vector 1 was 0.615. The addition of texture information improved the kappa coefficient by 0.15 for Vector 2. Even in the case of Vector 3 using VV-only polarization and Vector 4 using VH-only polarization, adding texture information improved the flooded area detection accuracy compared to the results for Vector 1. Therefore, the accuracy of flooded area detection could be improved by adding texture information to backscattering changes.

Direct comparison of flood detection accuracies obtained using a simple thresholding method with Sentinel-1 data [9] is not feasible as it relies on flooded area calculations derived exclusively from the paddy fields in Indonesia using PlanetScope's normalized difference water index. However, even when built-up

areas were included, the kappa coefficient improved, suggesting the effectiveness of applying machine learning along with this approach and the utility of using texture information.

The GRD image exhibits speckle noise corresponding to its effective number of looks, which is 4.3–4.4 for Sentinel-1 IW mode data [28]. Because the GLCM texture information considers the pixel value changes due to speckle noise in the calculation window, increasing the GLCM window size may improve the flood detection accuracy.

B. Detection Accuracy of the Flooded Area in Each Category

On comparing the F-values of each category shown in Table II, the F-value of the flooded built-up area was lower than that of the other categories in the test area. However, in the training area, the F-value of the flooded built-up areas was relatively high. These results suggested that the complexity of backscattering changes due to flooding in the built-up areas may be the reason for the lower F-values in the test area.

The F-value for Vector 3 (VV-only) was higher in the flooded built-up areas, while that for Vector 4 (VH-only) was higher for the flooded paddy fields, indicating that VV polarization was effective in improving the detection accuracy for flooded built-up areas, whereas VH polarization was effective in improving the detection accuracy of flooded paddy fields. Furthermore, double-bounce scattering caused changes in the backscattering coefficients in built-up areas, a combination of specular reflection of the water surface and surface scattering of the building wall. This change was consistent with the fact that double-bounce scattering is significant for co-polarization. For the flooded paddy fields, backscattering changes appeared prominently in cross polarization, as this study focused on the status of rice fields just before harvesting.

C. Effect of Scaling on the Flood Detection Accuracy

Regarding the calculated window size for the GLCM elements, a larger window size indicated higher detection accuracy for flooded areas. However, the number of gray levels that demonstrated the highest accuracy in the test area varied significantly (see Table II). Table III summarizes the kappa coefficients in the test area related to the window size and gray levels. According to Table III, the combination of window size and gray level gives the highest flood area detection accuracy as follows: window size of 19 × 19 and gray level of 8 for Vector 2, window size of 19 × 19 and gray level of 2 for Vector 3, and window size of 19 × 19 and gray level of 16 for Vector 4. Although many gray levels were expected to show a better detection accuracy, the results differed. Therefore, scaling while calculating the GLCM was adjusted for each polarization, and the detection accuracy was recalculated.

By excluding the top and bottom 1% of values and calculating the minimum and maximum values for each polarization, the VV polarization ranged from −17.1 to 7.1 dB, and the VH polarization ranged from −28.6 to 4.7 dB. Table IV summarizes the accuracy of detecting flooded area after scaling was adjusted. Fig. 9 shows the corresponding classified images listed in Table IV. After the scale change, both the dual and single

TABLE IV
SUMMARY OF FLOOD DETECTION ACCURACIES FOR VECTORS 1–4 AFTER ADJUSTING SCALING FOR EACH POLARIZATION

Vector				1	2	3	4
				γ^0	γ^0+Texture	γ^0+Texture	γ^0+Texture
				VV+VH	VV+VH	VV	VH
Training area	Kappa			0.762	0.960	0.922	0.852
	F1	Flooded areas	paddy	0.882	1.000	0.994	0.991
			built-up	0.793	0.943	0.905	0.790
		Nonflooded areas	paddy	0.820	0.998	0.969	0.922
			built-up	0.789	0.940	0.897	0.845
Test area	Kappa			0.616	0.734	0.648	0.702
	Gray level Window size			—	16 15×15	16 19×19	16 19×19
	F1	Flooded areas	paddy	0.752	0.845	0.712	0.887
			built-up	0.513	0.580	0.602	0.513
		Nonflooded areas	paddy	0.756	0.859	0.777	0.842
			built-up	0.752	0.823	0.793	0.772

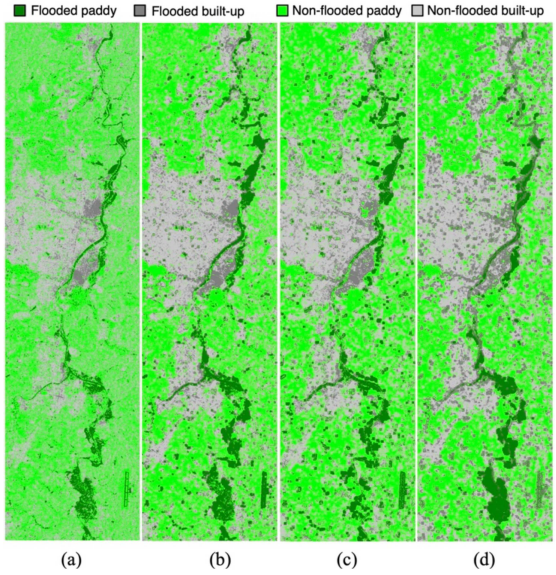

Fig. 9. Classified images with the highest flood detection accuracies after adjusting scaling for each polarization. (a) Vector 1. (b) Vector 2. (c) Vector 3. (d) Vector 4.

polarizations achieved their maximum classification accuracy at 16 gray levels. However, a comparison of kappa coefficients of the test areas in Tables II and IV indicates a slight decrease in detection accuracy. This decrease may be attributed to the scale change of each polarization, which increased the variability of γ^0 in the target area due to speckle noise present in polarization data. Consequently, the scale change for each polarization did not improve the detection accuracy.

V. CONCLUSION

In this study, flooded areas in built-up areas and paddy fields in Koriyama City, Fukushima Prefecture, were detected using changes in the backscattering coefficient and texture information from Sentinel-1 data acquired before and during flooding caused by Typhoon Hagibis in 2019. The combination of backscattering change and texture information improved the accuracy of flooded area detection by a kappa coefficient of approximately 0.15, compared to backscattering change-only information. Furthermore, comparison of the F-values for each category using dual- and single-polarization data confirmed that VV and VH polarization improved flooded area detection in built-up and paddy areas, respectively. The proposed approach successfully

detects flood-damaged areas caused by Typhoon Hagibis in both the built-up and paddy areas and, thus, can be applied to evaluate the impacts of future flood disasters.

In future, we aim to enhance flood area detection accuracy by exploring additional textural features beyond entropy. This exploration will involve identifying optimal gray levels and window sizes to achieve the maximum detection accuracy.

ACKNOWLEDGMENT

The European Space Agency provided the Sentinel-1 SAR data used in this study.

REFERENCES

[1] "Damage of typhoon no. 19," Koriyama City. Accessed: Sep. 15, 2023. [Online]. Available: https://www.city.koriyama.lg.jp/uploaded/attachment/26720.pdf
[2] "Agriculture and forestry news." Accessed: Sep. 15, 2023. [Online]. Available: https://www.pref.fukushima.lg.jp/uploaded/attachment/372719.pdf
[3] "Mainichi news." Accessed: Sep. 15, 2023. [Online]. Available: https://mainichi.jp/articles/20191018/ddl/k07/040/036000c
[4] H. Wakabayashi, T. Igarashi, and S. Tsukamoto, "Flood damage analysis in Koriyama City caused by typhoon Hagibis using Sentinel-1 SAR data," in *Proc. Int. Geosci. Remote Sens. Symp.*, 2022, pp. 6021–6024, doi: 10.1109/IGARSS46834.2022.9884430.
[5] M. Arii, "Sensitivity study of ALOS-2 data to floodwaters in Joso City in 2015 and its application," *J. Remote Sens. Soc. Jpn.*, vol. 38, no. 4, pp. 325–336, 2018, doi: 10.11440/rssj.38.325.
[6] L. Pulvirenti, M. Chini, N. Pierdicca, and G. Boni, "Use of SAR data for detecting floodwater in urban and agricultural areas: The role of the interferometric coherence," *IEEE Trans. Geosci. Remote Sens.*, vol. 54, no. 3, pp. 1532–1544, Mar. 2016, doi: 10.1109/TGRS.2015.2482001.
[7] J.-B. Henry, P. Chastanet, K. Fellah, and Y.-L. Desnos, "Envisat multi-polarized ASAR data for flood mapping," *Int. J. Remote Sens.*, vol. 27, no. 10, pp. 1921–1929, 2006, doi: 10.1080/01431160500486724.
[8] S. Martinis, A. Twele, and S. Voigt, "Towards operational near real-time flood detection using a split-based automatic thresholding procedure on high resolution TerraSAR-X data," *Natural Hazards Earth Syst. Sci.*, vol. 9, no. 2, pp. 303–314, 2009, doi: 10.5194/nhess-9-303-2009.
[9] H. Wakabayashi, C. Hongo, T. Igarashi, Y. Asaoka, B. Tjahjono, and I. R. R. Permata, "Flooded rice paddy detection using Sentinel-1 and PlanetScope data: A case study of the 2018 spring flood in west Java, Indonesia," *IEEE J. Sel. Topics Appl. Earth Observ. Remote Sens.*, vol. 14, pp. 6291–6301, 2021, doi: 10.1109/JSTARS.2021.3083610.
[10] S. Martinis, J. Kersten, and A. Twele, "A fully automated TerraSAR-X based flood service," *ISPRS J. Photogrammetry Remote Sens.*, vol. 104, pp. 203–212, 2015, doi: 10.1016/j.isprsjprs.2014.07.014.
[11] L. Pulvirenti, M. Chini, N. Pierdicca, L. Guerriero, and P. Ferrazzoli, "Flood monitoring using multi-temporal COSMO-SkyMed data: Image segmentation and signature interpretation," *Remote Sens. Environ.*, vol. 115, no. 4, pp. 990–1002, 2011, doi: 10.1016/j.rse.2010.12.002.
[12] A. Twele, W. Cao, S. Plank, and S. Martinis, "Sentinel-1-based flood mapping: A fully automated processing chain," *Int. J. Remote Sens.*, vol. 37, no. 13, pp. 2990–3004, 2016, doi: 10.1080/01431161.2016.1192304.
[13] A. Refice et al., "SAR and InSAR for flood monitoring: Examples with COSMO-SkyMed data," *IEEE J. Sel. Topics Appl. Earth Observ. Remote Sens.*, vol. 7, no. 7, pp. 2711–2722, Jul. 2014, doi: 10.1109/JSTARS.2014.2305165.
[14] M. Chini, R. Pelich, L. Pulvirenti, N. Pierdicca, R. Hostache, and P. Matgen, "Sentinel-1 InSAR coherence to detect floodwater in urban areas: Houston and Hurricane Harvey as A test case," *Remote Sens.*, vol. 11, no. 2, 2019, Art. no. 107, doi: 10.3390/rs11020107.
[15] M. Ohki et al., "Flood area detection using PALSAR-2 amplitude and coherence data: The case of the 2015 heavy rainfall in Japan," *IEEE J. Sel. Topics Appl. Earth Observ. Remote Sens.*, vol. 12, no. 7, pp. 2288–2298, Jul. 2019, doi: 10.1109/JSTARS.2019.2911596.
[16] R. M. Haralick, K. Shanmugam, and I. Dinstein, "Textural features for image classification," *IEEE Trans. Syst., Man, Cybern.*, vol. SMC-3, no. 6, pp. 610–621, Nov. 1973, doi: 10.1109/TSMC.1973.4309314.
[17] H. Sohn, Y. S. Song, and G. H. Kim, "Detecting water area during flood event from SAR image," in *Computational Science and Its Applications*, vol. 3481. New York, NY, USA: Springer, 2005, pp. 771–780.
[18] A. Dasgupta, S. Grimaldi, R. Ramsankaran, and J. P. Walker, "Optimized GLCM-based texture features for improved SAR-based flood mapping," in *Proc. IEEE Int. Geosci. Remote Sens. Symp.*, 2017, pp. 3258–3261, doi: 10.1109/IGARSS.2017.8127692.
[19] "Inundation depth map in Koriyama City." Accessed: Sep. 15, 2023. [Online]. Available: https://www.gsi.go.jp/BOUSAI/R1.taihuu19gou.html#11
[20] "Aerial photographs of flooded area caused by typhoon hagibis by geospatial information authority of Japan." Accessed: Sep. 15, 2023. [Online]. Available: https://www.gsi.go.jp/BOUSAI/R1.taihuu19gou.html#6
[21] F. De Zan and A. Monti Guamieri, "TOPSAR: Terrain observation by progressive scans," *IEEE Trans. Geosci. Remote Sens.*, vol. 44, no. 9, pp. 2352–2360, Sep. 2006.
[22] A. S. Laliberte and A. Rango, "Texture and scale in object-based analysis of subdecimeter resolution unmanned aerial vehicle (UAV) imagery," *IEEE Trans. Geosci. Remote Sens.*, vol. 47, no. 3, pp. 761–770, Mar. 2009, doi: 10.1109/TGRS.2008.2009355.
[23] C. Cortes and V. Vapnik, "Support-vector networks," *Mach. Learn.*, vol. 20, no. 3, pp. 273–297, 1995, doi: 10.1007/BF00994018.
[24] A. E. Maxwell, T. A. Warner, and F. Fang, "Implementation of machine-learning classification in remote sensing: An applied review," *Int. J. Remote Sens.*, vol. 39, no. 9, pp. 2784–2817, 2018, doi: 10.1080/01431161.2018.1433343.
[25] G. Mountrakis, J. Im, and C. Ogole, "Support vector machines in remote sensing: A review," *ISPRS J. Photogrammetry Remote Sens.*, vol. 66, no. 3, pp. 247–259, 2011, doi: 10.1016/j.isprsjprs.2010.11.001.
[26] C.-C. Chang and C.-J. Lin, "LIBSVM : A library for support vector machines," *ACM Trans. Intell. Syst. Technol.*, vol. 2, no. 3, 2011, Art. no. 27, doi: 10.1145/1961189.1961199.
[27] C. A. Ramezan, T. A. Warner, and A. E. Maxwell, "Evaluation of sampling and cross-validation tuning strategies for regional-scale machine learning classification," *Remote Sens.*, vol. 11, no. 2, 2019, Art. no. 185, doi: 10.3390/rs11020185.
[28] "Sentinel-1 product definition." Accessed: Sep. 15, 2023. [Online]. Available: https://sentinels.copernicus.eu/documents/247904/1877131/Sentinel-1-Product-Definition.pdf

Takahiro Igarashi received the B.E. and M.E. degrees in computer science in 2019 and 2021, respectively, from Nihon University, Koriyama, Japan, where he is currently working toward the Ph.D. degree in computer science.

His research interests include machine learning techniques applied to high-resolution optical and microwave remote sensing data.

Hiroyuki Wakabayashi (Member, IEEE) received the B.S. and M.S. degrees in electronics engineering in 1981 and 1983, respectively, and the Ph.D. degree in applied physics in 1996, all from Hokkaido University, Sapporo, Japan.

In 1983, he joined the National Space Development Agency of Japan (currently Japan Aerospace Exploration Agency), Tokyo, Japan. He worked on data processing and Cal/Val systems for JERS-1 from 1986 to 1991 and the ALOS/PALSAR conceptual design from 1994 to 1999. He was a Research Scientist with the Earth Observation Research Center and engaged in polarimetric synthetic aperture radar (SAR) research from 1999 to 2006. From 2001 to 2003, he stayed at the Syowa Station, where he was in charge of SAR data processing and analysis for sea ice monitoring. From 2006 to 2024, he was a Professor of Computer Science with the College of Engineering, Nihon University, Koriyama, Japan. In 2024, he joined Tohoku Gakuin University, Sendai, Japan, where he is currently a Professor with the Graduate School of Human Informatics.

Dr. Wakabayashi is a Member of the Institute of Electronics, Information and Communication Engineers, the Remote Sensing Society of Japan, the Japan Society of Photogrammetry and Remote Sensing, and the Japanese Society of Snow and Ice. He was a member of the 43rd Japanese Antarctic Research Expedition.